

COMPRESSIBLE MULTICOMPONENT FLOW CALCULATIONS AND SHOCK-BUBBLE INTERACTION

Eric Johnsen

Division of Engineering and Applied Science
California Institute of Technology
Pasadena, CA 91125
email: ejohnsen@caltech.edu

Tim Colonius

Division of Engineering and Applied Science
California Institute of Technology
Pasadena, CA 91125
email: colonius@caltech.edu

ABSTRACT

We report on the development of a numerical method to simulate two-dimensional compressible multicomponent flows. Our scheme is shock- and interface-capturing, quasi-conservative and high-order accurate. We validate it for two-dimensional problems including shock-bubble interactions and examine the shock-induced asymmetric collapse of a cylindrical gas bubble in water, where wave strengths and pulse durations are chosen to model conditions relevant to shockwave lithotripsy. In particular, we determine how the pressure at the surface of a nearby wall depends on the various properties of the pulse and on the geometry. We also describe the extension of the method to axisymmetric geometry and show preliminary results.

BACKGROUND

Cavitation erosion has been studied for many years, in an attempt to understand the structural damage observed on propeller blades, turbomachinery and hydraulic equipment [7, 9]. Early analysis has focused on spherical bubble dynamics, which are well described by the Rayleigh-Plesset equation [35, 38]. However, if an asymmetry is present in the flow field (e.g., solid boundary [4, 28, 36], gravity field [49]), the collapse is no longer spherical. In the case of the collapse of a bubble near a solid surface, a re-entrant jet directed towards the surface forms and penetrates the bubble. It was thought that the direct impact of the jet onto the wall was the primary cause of damage. Recent studies using high-speed cameras [22, 32, 48] indicate that cavitation erosion consists of a more elaborate process, as illustrated by the complex shockwave pattern during and after collapse.

Cavitation erosion has also been utilized in medical applications. For instance, in shockwave lithotripsy (SWL), shockwaves are focused on kidney stones, in order to break them. Although the stone comminution mechanism is not yet fully understood, it

has been shown that cavitation plays an important role [3, 11, 34]. Because of the difficulty in making controlled experimental measurements, numerical simulations are useful to provide a better understanding of the underlying mechanism of cavitation erosion.

To this end, we consider the two-dimensional shock-induced collapse of a single gas bubble near a solid surface and characterize the pressure generated on the wall. In this paper, we first briefly describe our numerical method [19] and validate it using two-dimensional shock-bubble interactions. Next, we study the collapse of a cylindrical bubble subjected to a typical lithotripter pulse. We then describe the implementation of the method in axisymmetric problems. We end by summarizing our findings and providing an outlook for future research.

MODEL EQUATIONS

The main features of the flows of interest are interactions between different types of waves and interfaces. Therefore, in order to simplify the model, we assume that the different fluid components are immiscible, and neglect viscous and thermal diffusion, surface tension and phase change. We thus consider the two-dimensional Euler equations,

$$\mathbf{q}_t + \mathbf{f}(\mathbf{q})_x + \mathbf{g}(\mathbf{q})_y = \mathbf{0}, \quad (1)$$

where $\mathbf{q} = (\rho, \rho u, \rho v, E)^T$ is the vector of conserved quantities, density, momentum (in x and y) and total energy, and $\mathbf{f} = (\rho u, \rho u^2 + P, \rho uv, u(E + P))^T$ and $\mathbf{g} = (\rho v, \rho uv, \rho v^2 + P, v(E + P))^T$ are the flux vectors. The system is closed by specifying a relationship between the pressure and the energy. A stiffened

equation of state [17] appropriate for gases and liquids is used,

$$\Gamma P + \Pi_\infty = E - \rho \frac{u^2 + v^2}{2}, \quad (2)$$

where $\Gamma = 1/(\gamma - 1)$ and $\Pi_\infty = \gamma P_\infty/(\gamma - 1)$. For perfect gases, γ is the ratio of specific heats and $P_\infty = 0$; for water, γ and P_∞ are determined from Hugoniot data [10]. Interfaces between different fluids are represented by a discontinuity in the properties, γ and P_∞ . Since material interfaces are advected by the flow, Γ and Π_∞ obey the advection equation [1, 43],

$$\phi_t + u\phi_x + v\phi_y = 0, \quad (3)$$

where $\phi = (\Gamma, \Pi_\infty)^T$. Equations (1) and (3) form a quasi-conservative system [43], so that ρ , ρu and E are conserved, while Γ and Π_∞ are advected. We note that the advection equations could be rewritten in conservative form using the continuity equation; however, solving such a system of equations numerically would generate oscillations near interfaces, as explained in the next sections.

NUMERICAL SCHEME

Compressible multicomponent flows

Early numerical simulations of the collapse of a single bubble near a solid wall were performed using Lagrangian methods based on potential flow theory [6, 36]. Although such formulations capture the initial deformations well, the latter stages of the collapse are not always accurately represented, as the assumptions of incompressibility and irrotationality of the flow are no longer valid. Furthermore, the topological change that occurs as the jet impacts the distal side of the bubble must be handled with care in such methods [5].

Efforts to simulate compressible multicomponent flows have focused on shock-capturing schemes. However, early algorithms often produced interface oscillations [20, 27]. The cause of these oscillations is identified in [1], where a quasi-conservative formulation is proposed for gases. This has subsequently been extended to more general equations of state [43]. These schemes are low-order accurate, so that they are not well-suited to problems where complex smooth regions interact with discontinuities [42]. The Ghost Fluid Method [15] is one method for solving standard multicomponent flows where high-order differencing schemes can be implemented. The interface is tracked using a level set function [30], so that it is sharp; ghost cells are provided to complete stencils across interfaces, so that no spurious oscillations are generated. However, (discrete) conservation errors occur when strong shockwaves interact with interfaces [25], which is likely to happen in the problems of interest.

In order to measure the quantities relevant to our study, the entire flow field must be reconstructed. The numerical method must be robust in order to handle strong shockwaves and interfaces separating fluid components of very large density ratios. In addition, high-order accuracy is required to resolve the complex smooth features of the flow. We therefore follow the quasi-conservative approach taken in [1, 43] and extend it to high-order accuracy. The full two-dimensional Euler equations are solved using a shock-capturing scheme, and the properties defining the fluid components (*i.e.*, Γ and Π_∞) are advected in a consistent fashion. In this formulation, interfaces are not explicitly tracked, but rather captured; they are allowed to diffuse according to the numerical viscosity of the scheme, in a manner similar to that of shockwaves. No spurious interface oscillations are observed, even though very large density ratio (1000:1) are considered, and the method is high-order accurate.

Time-marching and spatial discretization

The time-marching and spatial discretization are based on standard high-order accurate shock-capturing schemes. A third-order accurate TVD Runge-Kutta scheme [41] marches the equations forward in time. The spatial discretization consists of a fifth-order accurate WENO reconstruction [18, 23], along with an HLLC approximate Riemann solver [47]; the reconstruction is two-dimensional [46] and performed in characteristic space. For the two-dimensional shock-bubble interactions, we set $\Delta t/\Delta x = 0.2$ and the spatial resolution is 800×400 (600×150 for the axisymmetric case); for the lithotripsy problem, $\Delta t/\Delta x = 0.5$ and the spatial resolution is 400×200 . The grid is uniform in all cases. However, our scheme features several critical differences from the standard schemes, as explained in the next sections.

Spurious interface oscillations

When standard shock-capturing schemes are used to solve the system of equations (1) and (3), spurious oscillations are generated at interfaces, if proper care is not taken [20, 27]. This happens even in the simple case of the advection of a material interface. To solve this particular problem using WENO schemes, we have shown that a finite volume formulation must be adopted, where the adequately averaged primitive variables are reconstructed, not the usual conservative variables [19]. Furthermore, the discretization of the advection equations must be consistent with the energy equation. We therefore adapted the HLLC solver to the advection equation [19]. Finally, the specific functions, $\Gamma = 1/(\gamma - 1)$ and $\Pi_\infty = \gamma P_\infty/(\gamma - 1)$, must be advected, not just any function of γ and P_∞ [43].

This reconstruction is no more difficult to implement than the usual WENO reconstruction of the conservative variables, and it preserves the total momentum and energy in each computational cell [19]. Since the Euler equations are in flux-difference form, the numerical scheme is discretely conservative [21].

Using this formulation, the method does not generate oscillations at isolated shockwaves, interfaces and rarefaction waves. We have shown using numerical examples that no oscillations are generated when shockwaves interact with interfaces in one and two dimensions, that mass, momentum and energy are conserved to round-off errors, and that the scheme shows proper convergence [19].

Reconstruction of the primitive variables

The reconstruction of the appropriately averaged primitive variables is a key feature of our method. We define a local average velocity, \bar{w} , and pressure, \bar{p} , in one dimension for simplicity:

$$\bar{w}_j = \frac{\bar{\rho} \bar{u}_j}{\bar{\rho}_j}, \quad \bar{p}_j = \frac{\bar{E}_j - \bar{\rho}_j \frac{\bar{w}_j^2}{2} - \bar{\Pi}_{\infty,j}}{\bar{\Gamma}_j}, \quad (4)$$

where the cell-average value of a function, f , is defined as

$$\bar{f}_j = \frac{1}{\Delta x} \int_{x_j - \Delta x}^{x_j + \Delta x} f(x) dx. \quad (5)$$

The density-weighted velocity is reminiscent of Favre averages in compressible turbulence models [14]. This methodology does not deteriorate the overall order of accuracy of the scheme, as the function, $\bar{w}(x)$, approximates the exact velocity, $u(x)$, to the same order of accuracy as the function, $\bar{u}(x)$, does [19]. The same holds for the pressure. This property is also important for the axisymmetric implementation and is examined more closely in the last section.

SHOCK-BUBBLE INTERACTIONS

Air-He

The two-dimensional shock-bubble interaction [16] has become a benchmark problem for compressible multicomponent flows. We use it as a validation case and as an example of the importance of preventing spurious interface oscillations.

A Mach 1.22 shockwave in air ($\rho_{\text{air}} = 1$, $\gamma_{\text{air}} = 1.4$) interacts with a helium ($\rho_{\text{He}} = 0.138$, $\gamma_{\text{He}} = 1.67$) cylinder. Reflecting boundary conditions are specified on the top and along the centerline, and nonreflecting boundary conditions [45] on the left and right. In Figures 1 and 2, we present idealized Schlieren contours [37] and density lines to visualize the general wave structure and the details of the flow, using the present scheme and a WENO scheme where the full conservative variables are reconstructed.

Our results are in good qualitative agreement with past experimental [16] and numerical [26, 33, 37] findings, as both

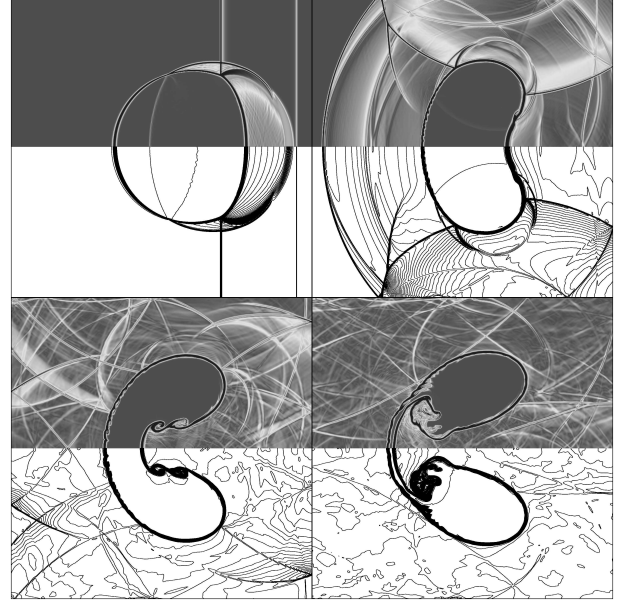


Figure 1. Mach 1.22 shockwave in air hitting a helium cylinder, using the present scheme. Top half: idealized Schlieren; bottom half: density lines.

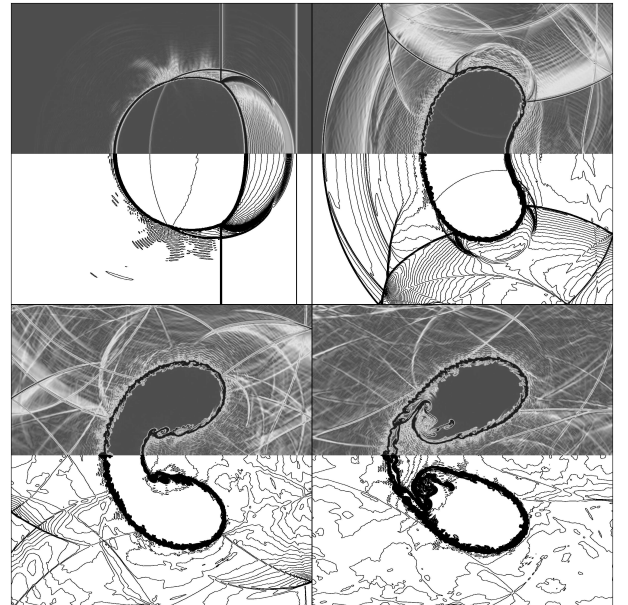


Figure 2. Mach 1.22 shockwave in air hitting a helium cylinder, using a fully conservative scheme. Top half: idealized Schlieren; bottom half: density lines.

shockwaves and interfaces are well resolved. The first wave interactions and the subsequent reflections off the wall are well captured. The Kelvin-Helmholtz instability that develops along

the interface and the jet formation due to the baroclinic torque are consistent with previous findings.

The fully conservative scheme clearly generates unacceptable oscillations, even before the shockwave reaches those areas. Their main dynamical effect is to perturb the interface, so that the Kelvin-Helmholtz instability is triggered sooner than expected. As a result, the interface becomes more smeared, which causes a decrease in the strength of the wave fronts that pass through it. This is not the case when the present scheme is used. We note in passing that the start-up error in the form of an entropy wave is generated when the shockwave is started [2]; however, this has no dynamical effect on the field.

Water-air

We consider the two-dimensional interaction of a Mach 1.67 shockwave in water ($\rho_{\text{water}} = 1$, $\gamma_{\text{water}} = 5.17$, $P_{\infty, \text{water}} = 0.19$) hitting an air ($\rho_{\text{air}} = 0.001$) cylinder [24]. This problem is similar to experiments by [8], where cavities in a water/gelatin mixture are impacted by a shockwave. In Figure 3, we again plot idealized Schlieren contours [37] and density lines.

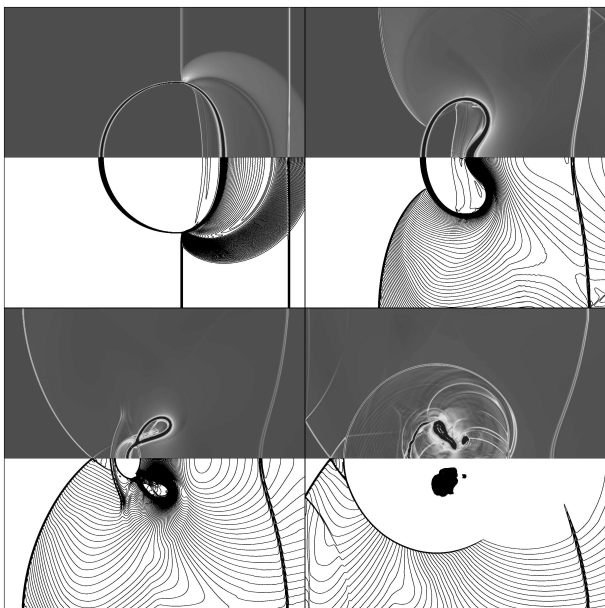


Figure 3. Mach 1.67 shockwave in water hitting an air cylinder. Top half: idealized Schlieren; bottom half: density lines.

Although the bubble initially deforms in a fashion similar to the air/He case, it collapses to a smaller size, under the effect of the large pressure. The re-entrant jet formed due to the baroclinic torque has greater momentum than previously, since it consists of water. As it impacts the distal side of the bubble, a large water-hammer pressure is generated. Thereafter, a secondary re-entrant

jet forms in the opposite direction. As a result, the bubble is broken up into four pieces [29].

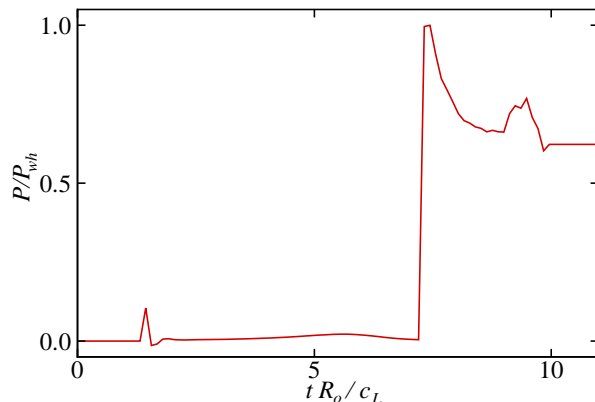


Figure 4. History of the pressure at the tip of the jet.

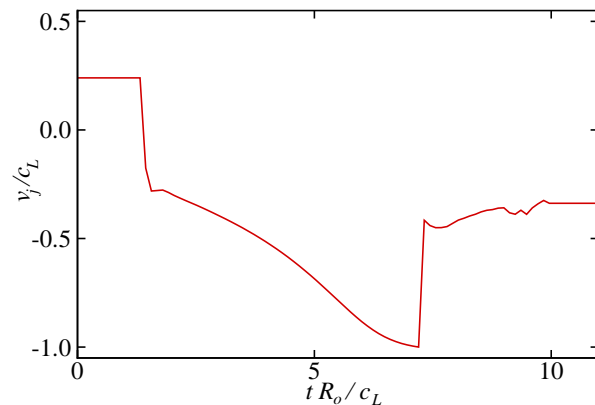


Figure 5. History of the local speed at the tip of the jet.

The water-hammer pressure and jet velocity are of great interest in this study. Figures 4 and 5 show the history of the local normalized pressure and velocity at the tip of the jet, respectively. The variables are non-dimensionalized using the initial water density, ρ_L , and sound speed, c_L , and the initial bubble radius, R_0 .

The violence of the phenomenon is evident from the large jump in jet pressure and speed. The water-hammer pressure is almost an order of magnitude larger than the initial shockwave, which is expected because of the high-velocity jet. However, as the wave propagates radially, the front weakens. Similarly to Sedov's blast wave problem [40], a finite amount of energy is generated at the point of impact of the jet on the distal side of the

bubble. As this pressure wave propagates radially outward, the area over which it acts increases while the energy remains constant, so that the amplitude of the pressure front decreases. This is further illustrated in Figure 6, which shows the pressure at several points along the left boundary of the computational domain; the bottom set refers to the pressure measured along the centerline, the middle to a point two units above and the top to a point four units above (the top boundary is located five units above the centerline). Nevertheless, far downstream, the magnitude of the water-hammer pressure is still considerable.

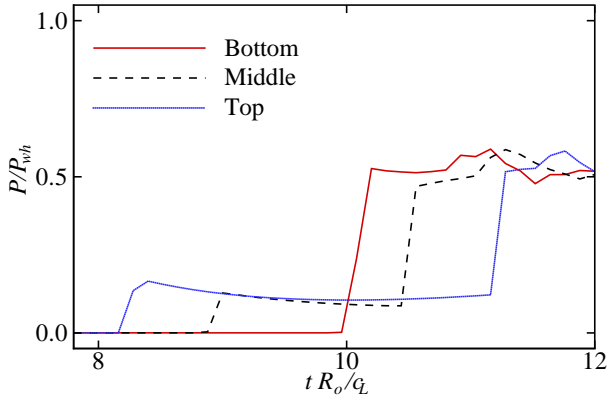


Figure 6. Pressure measurement along the left side of the domain.

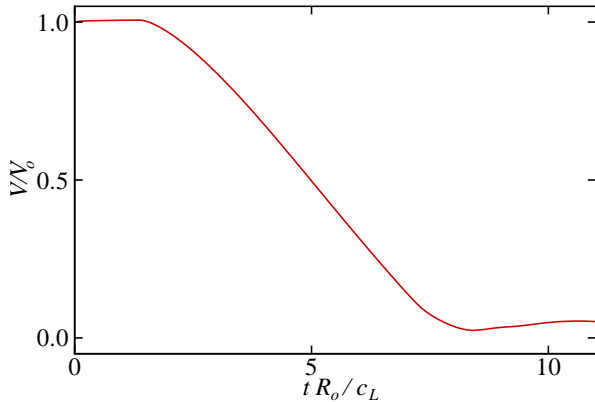


Figure 7. History of the bubble volume.

In this particular problem, the pressure generated when the bubble reaches its minimum size [22] does not appear to be significant. By considering the history of the bubble volume in Figure 7, we observe that the bubble reaches its minimum size after

the occurrence of the water-hammer. This may still be of importance, as a second pressure peak is observed in Figures 4 and 6. However, several other events might also contribute to this pressure: the water-hammer due to a secondary re-entrant jet and the collision of shockwaves formed during the first water-hammer.

SWL PROBLEM

We consider the collapse of a cylindrical bubble subjected to a lithotripter pulse. The purpose of this study is to determine how the pressure along a nearby surface depends on the certain properties of the pulse and on the geometry. Because the simulation is two-dimensional and because higher-resolution runs are impractical due to long run-times, the results are analyzed in a qualitative fashion only and compared to previous work [12, 31, 39, 50]. These comparisons prove to be difficult, because the results depend on the lithotripter specifications; nevertheless, we are able to verify certain trends.

Problem set-up

For a given reference bubble radius, R_o , the relevant properties of the pulse are the waveform, the amplitude, P/P_o , and the relative width, σ/R_o . The geometry is characterized by the stand-off distance from the end-wall, H/R_o , and the distance from the side-wall, S/R_o . The effect of each feature is considered by isolating it, so that the other parameters do not affect the problem. For simplicity, the bubble is assumed to be in equilibrium with its surroundings before the pulse reaches it; if the bubble were oscillating, the resulting behavior would be quite different [39]. The problem set-up is shown in Figure 8.

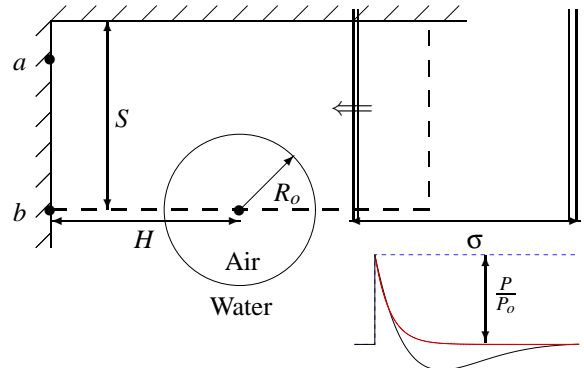


Figure 8. Schematic of the SWL problem.

Several waveforms are relevant to this study: a shockwave (dashed line), the Church profile (solid line), and a shockwave followed by an exponentially decaying expansion (dotted line).

A typical lithotripter pulse has a Church waveform, consisting of a shockwave of amplitude of 35 MPa, followed by a long expansion to a negative pressure of -10 MPa, which then returns to atmospheric pressure. The pulse-width is defined as the length from the shock to the point where the pressure is back to atmospheric, after having gone negative, which is about 6.75 mm. Since the current model does not include cavitation, a shockwave followed by an expansion exponentially decaying to atmospheric pressure is used instead. This pulse is designed so that it initially matches the decay of the Church profile. Initial bubble radii are approximately 50 μm . These parameters constitute the typical lithotripsy problem mentioned in the next sections.

As a measure of structural damage, the pressure is recorded on the left side of the computational domain near the top (point *a*) – at a height of two bubble radii – and along the centerline (point *b*), as shown in Figure 8. The non-dimensionalization is performed using the initial water density, ρ_L , and speed of sound, c_L , and the initial bubble radius, R_o . In non-dimensional units, the length and height of the domain, are 5 and 2.5, respectively. Reflecting boundary conditions are used along the centerline and where there are walls, while incoming boundary conditions [45] are specified on the right boundary and non-reflecting boundary conditions are used elsewhere.

Overall qualitative behavior

In the cases studied here, the bubble behavior is close to that of the shock-bubble interaction in water. However, because the shockwave is much weaker, the baroclinic torque does not have as great an effect. The collapse time is much smaller than the characteristic time of the pulse, so that the collapse is initially approximately symmetric, as noted in [31]. As the bubble radius decreases and the interface accelerates, the asymmetry becomes more pronounced, so that a re-entrant jet forms and impacts the distal side, generating a radially propagating water-hammer pressure wave. The process is shown in Figure 9, where idealized Schlieren and pressure contours of a typical lithotripsy problem are shown; the interface is outlined in the pressure plot. A wall is located on the left boundary of the computational domain, and $H/R_o = 2.5$.

For this particular problem, our findings suggest that the strong pressure wave results from the water-hammer. We do not see clear indication that a pressure wave is emitted when the bubble reaches a minimum size, as may have been the case in the problems considered in [22]. We note that, because surface tension, phase change and diffusive effects are neglected, the collapse may appear stronger than it is in reality and the late-time behavior is approximate.

Effect of the stand-off distance from the wall

One of the goals of the study is to determine the dependence of the pressure measurements on the stand-off distance from the

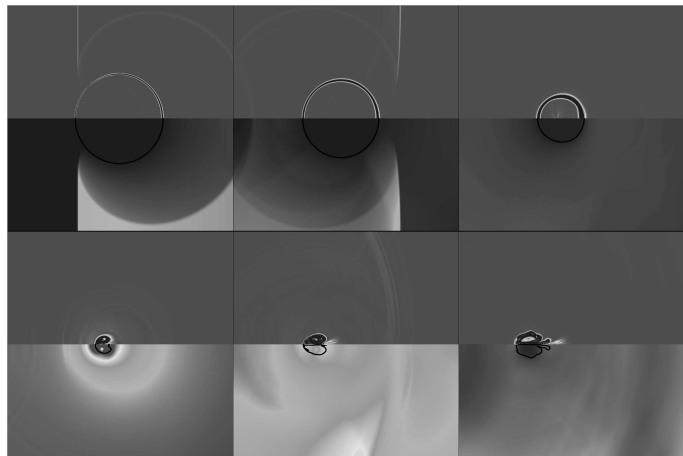


Figure 9. Collapse of a cylindrical bubble subjected to a typical lithotripter pulse. Top half: idealized Schlieren; bottom half: pressure contours (with interface outlined).

wall. The wall is placed on the left of the computational domain, and a typical lithotripsy problem is considered. The bubble is initially located at $H/R_o = 0, 1.5, 2.5, \infty$, with all the other parameters kept constant. For the case, $H/R_o = 0$, the bubble is actually a hemi-cylinder lying on the surface of the wall. For the case, $H/R_o = \infty$, the bubble was placed at the center of the computational domain, with non-reflecting wall boundary condition, to allow comparison with the other cases. Figures 10 and 11 show the pressure history at points, *a* and *b*, in Figure 8, respectively.

As one might expect, the pressure along the wall increases as the bubble is initially placed closer to the wall. Similarly to the shock-bubble interaction in water, the amplitude of the pressure front decreases as it propagates outwards, since a finite amount of energy has been generated by the impact of the jet on the distal side of the bubble. Nevertheless, the water-hammer pressure is still quite large compared to that of the initial pulse (which has amplitude, 0.013), even at point, *a*. It can be observed that a single bubble shields the wall from the initial pulse; a similar feature has been observed in [44] in the context of clouds of bubbles.

The water-hammer pressure wave reflects off the wall and then again off the bubble surface, as an expansion wave; however, the transmitted wave reflects off the other side of the bubble as a shockwave and hits the wall again. This behavior can be observed in the cases, $H/R_o = 1.5, 2.5$. Although smaller, the subsequent pressure peaks are still significant. The jet speed is plotted in Figure 12 as a function of time. It can be seen that its maximum value does not vary greatly with respect to the initial distance from the wall. This is to be expected, since the pulse properties are identical in all cases.

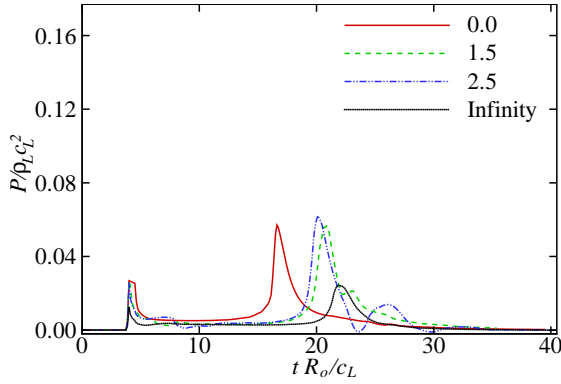


Figure 10. Pressure history at point, a , for various stand-off distances from the wall, for the SWL problem.

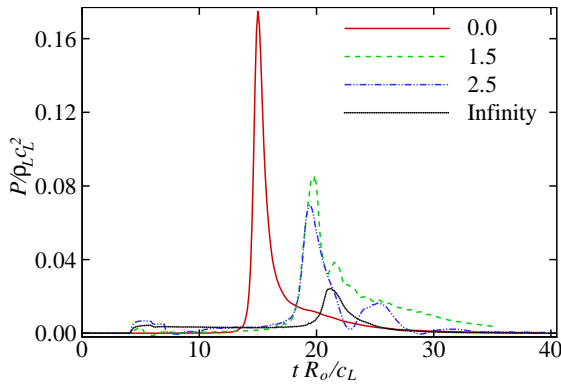


Figure 11. Pressure history at point, b , for various stand-off distances from the wall, for the SWL problem.

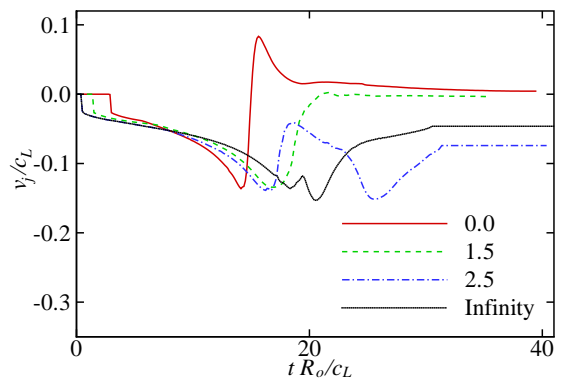


Figure 12. Jet speed for various stand-off distances from the wall, for the SWL problem.

Effect of the pulse-width

A second important parameter in this study is the pulse-width, relative to the bubble size. The bubble is placed at the

center of the domain (with no walls) and subjected to a typical lithotripter pulse. The following pulse-widths are considered: $\sigma/R_o = 67.5, 135, 675, \infty$. Figures 13 and 14 show the pressure history at points, a and b from Figure 8, respectively.

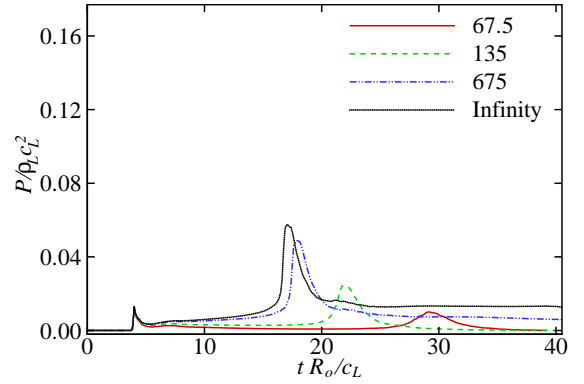


Figure 13. Pressure history at point, a , for various pulse-widths, for the SWL problem.

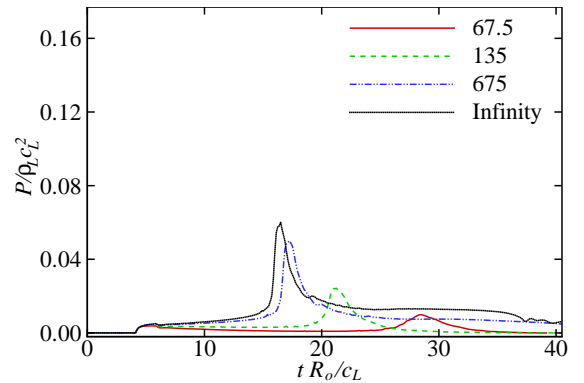


Figure 14. Pressure history at point, b , for various pulse-widths, for the SWL problem.

As the pulse-width is increased, the measured pressure increases. This is expected, since, for a fixed bubble size, the pulse resembles a shock for larger pulse-width and compresses the bubble steadily. The collapse time is smaller for longer pulse-widths, as the bubble “feels” a stronger effective pressure. This would not be the case for a Church profile, as discussed in [31]. The duration of the pulse also influences the jet speed, as shown in Figure 15: the maximum jet speed increases significantly as the pulse-width is increased.

These results can be interpreted from a different, but enlightening point of view. For a fixed pulse-width of $\sigma = 6.75$

mm, $\sigma/R_o = 67.5$ corresponds to a $100 \mu\text{m}$ radius bubble, and $\sigma/R_o = \infty$ corresponds to an infinitesimally small bubble, in which case any pulse looks like a shockwave. Therefore, the pressure measured on the wall is greater for smaller bubbles, which is confirmed by the Gilmore-based models of [12]. However, surface tension and viscous effects may be more important for small bubbles, thereby adding complexity to the problem.

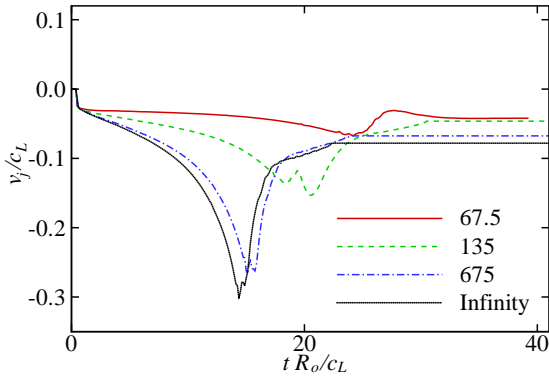


Figure 15. Jet speed for various pulse-widths, for the SWL problem.

Other effects

For the sake of conciseness, results for the effect of the amplitude of the pulse and that of side-walls are not shown in this study, but briefly summarized here. As one might expect, as the amplitude of the pulse is increased, larger pressures and jet speeds are observed. The presence of side-walls slows the collapse, as rarefaction waves are reflected back onto the bubble. A side-wall is equivalent to an identical image bubble. In reality, however, neighboring bubbles do not behave in phase and tend to gather [50].

AXISYMMETRIC IMPLEMENTATION

Although a three-dimensional extension of the present numerical method is trivial, its implementation is heavy on computer resources. Instead, an axisymmetric extension is considered, since many problems of interest have azimuthal symmetry.

Spatial discretization

In polar coordinates with azimuthal symmetry, the cell-averaged value of a function can be related to the cell-centered

value using Taylor series:

$$\frac{2\pi}{\Delta V_j} \int_{r_{j-1/2}}^{r_{j+1/2}} f(r) r dr = \frac{F_{j+1/2} - F_{j-1/2}}{r_j \Delta r} = f_j + O(\Delta r^2), \quad (6)$$

where $F' = fr$. However, we notice that the following expression also approximates the cell-centered value of f to the same order of accuracy:

$$\frac{1}{\Delta r} \int_{r_{j-1/2}}^{r_{j+1/2}} f(r) dr \frac{1}{r_j \Delta r} \int_{r_{j-1/2}}^{r_{j+1/2}} r dr = f_j + O(\Delta r^2). \quad (7)$$

This naturally leads us to defining a ‘‘linear’’ cell average value, as in Equation (5),

$$\bar{f}_j = \frac{1}{\Delta r} \int_{r_{j-1/2}}^{r_{j+1/2}} f(r) dr, \quad (8)$$

such that $f_j r_j = \bar{f}_j r_j + O(\Delta r^2) = \bar{f}_j \bar{r}_j + O(\Delta r^2)$. This follows the same idea as the appropriately averaged velocity and pressure described previously.

This formulation is important, because it allows us to rearrange the integral form of the Euler equation in the radial direction in the following semi-discrete fashion:

$$\frac{d}{dt} \bar{\rho}_j = - \frac{(\rho v)_{j+1/2} - (\rho v)_{j-1/2}}{\Delta r} - \frac{(\rho v)_{j+1/2} + (\rho v)_{j-1/2}}{2r_j}, \quad (9)$$

$$\frac{d}{dt} \bar{\rho} v_j = - \frac{(\rho v^2 + P)_{j+1/2} - (\rho v^2 + P)_{j-1/2}}{\Delta r} - \frac{(\rho v^2 + P)_{j+1/2} + (\rho v^2 + P)_{j-1/2}}{2r_j} + \frac{\bar{P}_j}{r_j}, \quad (10)$$

$$\frac{d}{dt} \bar{E}_j = - \frac{[v(E + P)]_{j+1/2} - [v(E + P)]_{j-1/2}}{\Delta r} - \frac{[v(E + P)]_{j+1/2} + [v(E + P)]_{j-1/2}}{2r_j}. \quad (11)$$

The geometrical source terms can therefore be treated using the same expression as the numerical fluxes. The only potential problem is the pressure term in the momentum equation. Recalling the previous discussion of the appropriately averaged pressure, we simply use the expression, $\bar{P}_j = \bar{p}_j$. Along $r = 0$, the equations are integrated over the zeroeth cell in a finite volume fashion, so that this reduces to a reflecting boundary condition.

Shock-bubble interaction

The axisymmetric implementation of our numerical method is tested for the spherical air-He shock-bubble interaction in [16], where $M = 1.25$. This has been studied numerically by [33] using a single-fluid model and by [13] using artificial viscosity; both methods are low-order accurate. In our simulation, the computational domain is a cylinder, as opposed to the square cross-section of the shock-tube test section of the experiment. Figure 16 shows idealized Schlieren contours and density lines for this process.

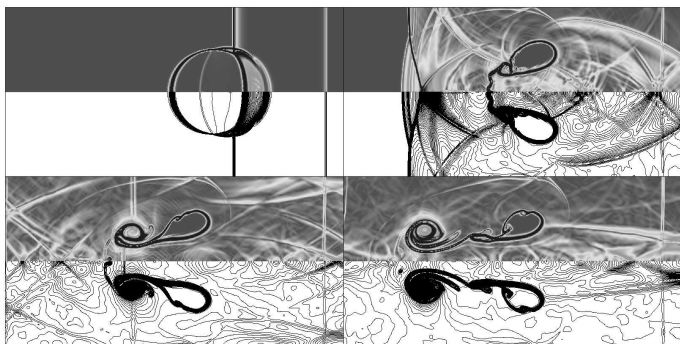


Figure 16. Mach 1.25 shockwave in air hitting a He sphere, using the axisymmetric implementation of our method. Top half: idealized Schlieren; bottom half: density lines.

Although these results are preliminary, they are in good qualitative agreement with the experiments of [16] and simulations of [13, 33]. The main difference with respect to the two-dimensional problem is the fact that the roll-up is faster and tighter, as remarked by [33], so that the vortex ring detaches from the main structure and convects downstream much sooner [16]. Because of this, the computational domain was extended, such that the resolution is not as high as for the two-dimensional problems.

CONCLUSIONS

We have shown that our numerical method is capable of simulating two-dimensional and axisymmetric compressible multi-component flow problems with large density ratio, such as the interaction of shockwaves in water with gas bubbles. In these problems, a re-entrant jet forms due to the baroclinic torque and impacts the distal side of the bubble, thereby generating a large water-hammer pressure. Secondary re-entrant jets are formed, breaking up the bubble into smaller pieces. The numerical method has been used to measure the pressure generated during the collapse of a cylindrical bubble subjected to a lithotripter pulse. It was found that larger pressures are measured when bubbles are initially located closer to the walls. Furthermore, for a

given pulse-width, smaller bubbles generate larger pressures and jet speeds.

An axisymmetric extension of the lithotripsy problem will allow the characterization of the stresses along the walls in a quantitative way. This will provide the basis for a more accurate damage model based on the bubble dynamics. Such high-order accurate simulation of compressible multi-component flows constitutes a first step in studying more general multiphase flow phenomena, where phase change, diffusive effects and surface tension are also important.

ACKNOWLEDGMENT

This work was supported by NIH grant PO1 DK043881.

REFERENCES

- [1] R. Abgrall, How to prevent pressure oscillations in multi-component flow calculations: a quasi conservative approach, *J. Comput. Phys.* **125**, 150 (1996).
- [2] M. Arora and P. L. Roe, On postshock oscillations due to shock capturing schemes in unsteady flows, *J. Comput. Phys.* **130**, 25 (1997).
- [3] M. R. Bailey and Y. A. Pishchalnikov, O. A. Sapozhnikov, R. O. Cleveland, J. A. McAteer, N. A. Miller, I. V. Pishchalnikova, B. A. Connors, L. A. Crum, and A. P. Evan, Cavitation detection during shock-wave lithotripsy, *Ultrasound Med. Biol.* **31**, 1245 (2005)
- [4] T. B. Benjamin and A. T. Ellis, The collapse of cavitation bubbles and the pressures thereby produced against solid boundaries, *Philos. Trans. R. Soc. London Ser. A* **260** 221 (1966).
- [5] J. P. Best, The formation of toroidal bubbles upon the collapse of transient cavities, *J. Fluid Mech.* **251** 79 (1993).
- [6] J. R. Blake, B. B. Taib, and G. Doherty, Transient cavities near boundaries. Part 1. Rigid boundary, *J. Fluid Mech.* **170** 479 (1986).
- [7] J. R. Blake and D. C. Gibson Cavitation bubbles near boundaries, *Annu. Rev. Fluid Mech.* **19** 99 (1987).
- [8] N. K. Bourne and J. E. Field, Shock-induced collapse of single cavities in liquids, *J. Fluid Mech.* **244** 225 (1992).
- [9] C. E. Brennen, *Cavitation and Bubble Dynamics* (Oxford University Press, Oxford, 1995).
- [10] J. P. Cocchi, R. Saurel, and J. C. Loraud, Treatment of interface problems with Godunov-type schemes, *Shock Waves* **5**, 347 (1996).
- [11] L. A. Crum, Cavitation microjets as contributory mechanism for renal calculi disintegration in ESWL, *J. Urol.* **140**, 1587 (1988).
- [12] Z. Ding and S. M. Gracewski, Response of constrained and unconstrained bubbles to lithotripter shock wave pulses, *J. Acoust. Soc. Am.* **96** 3636 (1994).

- [13] Z. Ding and S. M. Gracewski, The behaviour of a gas cavity impacted by a weak or strong shock wave, *J. Fluid Mech.* **309** 183 (1996).
- [14] A. Favre, Equations des gaz turbulents compressibles, *J. Méch.* **2**, 361 (1965).
- [15] R. P. Fedkiw, T. Aslam, B. Merriman, and S. Osher, A non-oscillatory Eulerian approach to interfaces in multimaterial flows (the Ghost Fluid Method), *J. Comput. Phys.* **152**, 457 (1999).
- [16] J. F. Haas and B. Sturtevant, Interaction of weak shock waves with cylindrical and spherical gas inhomogeneities, *J. Fluid Mech.* **181**, 41 (1987).
- [17] F. Harlow and A. Amsden, Fluid Dynamics, Monograph LA-4700, Los Alamos National Laboratory, Los Alamos, NM, 1971.
- [18] G. S. Jiang and C. W. Shu, Efficient implementation of WENO schemes, *J. Comput. Phys.* **126**, 202 (1996).
- [19] E. Johnsen and T. Colonius, Implementation of WENO schemes in compressible multicomponent flow problems, *J. Comput. Phys.* accepted for publication (2006).
- [20] S. Karni, Multicomponent flow calculations by a consistent primitive algorithm, *J. Comput. Phys.* **112**, 31 (1994).
- [21] R. J. LeVeque, *Finite Volume Methods for Hyperbolic Problems* (Cambridge University Press, New York, 2002).
- [22] O. Lindau and W. Lauterborn, Cinematographic observation of the collapse and rebound of a laser-produced cavitation bubble near a wall, *J. Fluid Mech.* **479** 327 (2003).
- [23] X. D. Liu, S. Osher, and T. Chan, Weighted essentially non-oscillatory schemes, *J. Comput. Phys.* **115**, 200 (1994).
- [24] T. G. Liu, B. C. Khoo, and K. S. Yeo, The simulation of compressible multi-medium flow II. Applications to 2D underwater shock refraction, *Comput. Fluids* **30**, 315 (2001).
- [25] T. G. Liu, B. C. Khoo, and K. S. Yeo, Ghost fluid method for strong shock impacting on material interface, *J. Comput. Phys.* **190**, 651 (2003).
- [26] A. Marquina and P. Mulet, A flux-split algorithm applied to conservative models for multicomponent compressible flows, *J. Comput. Phys.* **185**, 120 (2003).
- [27] W. Mulder, S. Osher, and J. A. Sethian, Computing interface motion in compressible gas dynamics, *J. Comput. Phys.* **100**, 209 (1992).
- [28] C. F. Naudé and T. A. Ellis, On the mechanism of cavitation damage by non-hemispherical cavities in contact with a solid boundary, *Trans. ASME, J. Basic Eng.* **83** 648 (1961).
- [29] R. R. Nourgaliev, T. N. Dinh, and T. G. Theofanous, Adaptive characteristics-based matching for compressible multi-fluid dynamics, *J. Comput. Phys.* **213**, 500 (2006).
- [30] S. Osher and J. A. Sethian, Fronts propagating with curvature-dependent speed: Algorithms based on Hamilton-Jacobi formulations, *J. Comput. Phys.* **79**, 12 (1988).
- [31] A. Philipp, M. Delius, C. Scheffczyk, A. Vogel, and W. Lauterborn, Interaction of lithotripter-generated shock waves with air bubbles, *J. Acoust. Soc. Am.* **93** 2496 (1993).
- [32] A. Philipp and W. Lauterborn, Cavitation erosion by single laser-produced bubbles, *J. Fluid Mech.* **361** 75 (1998).
- [33] J. M. Picone and J. P. Boris, Vorticity generation by shock propagation through bubbles in a gas, *J. Fluid Mech.* **189** 23 (1988).
- [34] Y. A. Pishchalnikov, O. A. Sapozhnikov, M. R. Bailey, J. C. Williams, R. O. Cleveland, L. A. Crum, A. P. Evan, and J. A. McAteer, Cavitation bubble cluster activity in the breakage of kidney stones by lithotripter shockwaves, *J. Urol.* **17** 435 (2003).
- [35] M. S. Plesset, The dynamics of cavitation bubbles, *ASME J. Appl. Mech.* **16** 228 (1949).
- [36] M. S. Plesset and R. B. Chapman, Collapse of an initially spherical vapour cavity in the neighbourhood of a solid boundary, *J. Fluid Mech.* **47** 283 (1971).
- [37] J. J. Quirk and S. Karni, On the dynamics of a shock-bubble interaction, *J. Fluid Mech.* **318**, 129 (1996).
- [38] Lord Rayleigh, On the pressure developed in a liquid during the collapse of a spherical cavity, *Phil. Mag.* **34**, 94 (1917).
- [39] G. N. Sankin, W. N. Simmons, S. L. Zhu, and P. Zhong, Shock wave interaction with laser-generated single bubbles, *Phys. Rev. Lett.* **95**, 034501 (2005).
- [40] L. I. Sedov, *Similarity and Dimensional Methods in Mechanics* (Academic Press, New York 1959).
- [41] C. W. Shu and S. Osher, Efficient implementation of essentially non-oscillatory shock-capturing schemes, *J. Comput. Phys.* **77**, 439 (1988).
- [42] C. W. Shu, High-order finite difference and finite volume WENO schemes and discontinuous Galerkin methods for CFD, *Int. J. Comput. Fluid Dyn.* **17**, 107 (2003).
- [43] K. M. Shyue, An efficient shock-capturing algorithm for compressible multicomponent problems, *J. Comput. Phys.* **142**, 208 (1998).
- [44] M. Tanguay and T. Colonius, Progress in modeling and simulation of shock wave lithotripsy (SWL), In *Proceedings of the Fifth International Symposium on Cavitation*, Osaka, Japan, 2003.
- [45] K. W. Thompson, Time dependent boundary conditions for hyperbolic systems, *J. Comput. Phys.* **68**, 1 (1987).
- [46] V. A. Titarev and E. F. Toro, Finite-volume WENO schemes for three-dimensional conservation laws, *J. Comput. Phys.* **201**, 238 (2004).
- [47] E. F. Toro, M. Spruce, and W. Speares, Restoration of the contact surface in the HLL-Riemann solver, *Shock Waves* **4**, 25 (1994).
- [48] A. Vogel, W. Lauterborn, and R. Timm, Optical and acoustic investigations of the dynamics of laser-produced cavitation bubbles near a solid boundary, *J. Fluid Mech.* **206** 299 (1989).
- [49] J. K. Walters and J. F. Davidson, The initial motion of a

gas bubble formed in an inviscid liquid. Part 1. The two-dimensional bubble, *J. Fluid. Mech.* **12**, 408 (1962).

- [50] B. Wolfrum, T. Kurz, R. Mettin, and W. Lauterborn, Shock wave induced interaction of microbubbles and boundaries, *Phys. Fluids* **47**, 2916 (2003).